Linear and Nonlinear Dynamics of Relativistic Tori

Luciano Rezzolla

SISSA, International School for Advanced Studies, Trieste, Italy

INFN, Sezione di Trieste, Trieste, Italy

Abstract. I present results of two-dimensional general relativistic hydro-dynamical simulations of constant specific angular momentum tori orbiting around a Schwarzschild black hole. After introducing axisymmetric pertur-bations, these objects either become unstable to the runaway instability or respond with regular oscillations. The latter, in particular, are responsible for quasi-periodic bursts of accretion onto the black hole as well as for the emission of intense gravitational radiation, with signal-to-noise ratios at the detector which are comparable or even larger than the typical ones expected in stellar-core collapse.

1. Introduction

Stationary barotropic configurations around black holes in which the matter moves in circular orbits within isobaric equipotential surfaces have been studied for more than twenty years [1, 2]. An important feature of these non-Keplerian solutions is that the equipotential surfaces possess, in general, a sharp cusp on the equatorial plane, which behaves as an effective Lagrangian point, thus providing accretion even in the absence of a shear viscosity in the fluid. The dynamical response of these relativistic tori to perturbations has important astrophysical implications and will be discussed here in connection with the following three issues.

Firstly, the stability with respect to accretion of matter through the cusp. Any fluid element orbiting at the cusp will, upon experiencing the smallest inward radial perturbation, accrete onto the black hole. This will change the black hole mass, affect the stationary solution and, most importantly, the location of the cusp. The dynamics of the cusp can then have two possible evolutions. If, as a result of the newly accreted matter, the cusp moves to *smaller* radial positions, all fluid elements will be on *stable* circular orbits and no further accretion will be possible. If, on the other hand, the cusp moves to *larger* radial positions faster than the inner edge of the torus (which has shrunk as a result of the mass loss), the new configuration will *not* be of stable equilibrium and additional material can therefore accrete onto the black hole. The instability which is

produced in this way is then referred to as the "runaway" instability [3] and could have important implications on current models of γ-ray bursts [4, 5].

Secondly, the possibility of calculating numerically the linear and nonlinear hydrodynamical evolution of the torus provides a useful tool for relativistic disco-seismology in two dimensions. Having an internal structure governed by the balance of gravitational sources, pressure gradients and centrifugal forces, these relativistic tori possess non-trivial oscillation properties which are still essentially unexplored. By introducing perturbations, it is possible to excite the relevant modes of oscillations and calculate the characteristic eigenfrequencies to high accuracy and even in the absence of a perturbative analysis. Furthermore, during each of these oscillations a significant amount of matter could fall onto the black hole and, in a realistic scenario, it is reasonable to expect that before this matter reaches the event horizon, it will loose part of its binding energy, increase its temperature and emit electromagnetic radiation. For this reason, the quasi-periodic accretion produced in this way could be observed also in the form of a quasi-periodic X-ray luminosity [6].

Thirdly, and maybe most importantly, because of their toroidal topology, the relativistic tori considered here have intrinsically large mass quadrupoles and if the latter are induced to change rapidly as a consequence of perturbations or instabilities, large amounts of gravitational waves could be emitted and possibly detected [7, 8].

The plan of this paper is as follows: in Sections 2 and 3 I will first discuss briefly how stationary, non-Keplerian fluid configurations can be constructed and the numerical setup necessary to study their evolution in time. Section 4 is dedicated to a discussion of how to account for the changes in the spacetime geometry without an explicit solution of the Einstein equations, while in Section 5 I present the family of perturbations imposed on the equilibrium models. The numerical results are finally presented in Section 6, while the conclusions and the outlook for future developments are summarised in Section 7. Throughout, I will use a space-like signature $(-, +, +, +)$ and a system of geometrized units in which $G = c = 1$. The unit of length is chosen to be the gravitational radius of the black hole, $r_{\mathrm{g}} \equiv GM/c^2$, where M is the mass of the black hole. When useful, however, cgs units will be reported for clarity. Greek indices are taken to run from 0 to 3.

2. Stationary configurations

Stationary toroidal fluid configurations in a curved spacetime can be calculated after solving the Euler equations for a fluid in circular and non-Keplerian orbits. To this scope I consider a perfect fluid described by the stress-energy tensor

$$T^{\mu\nu} \equiv \rho h u^\mu u^\nu + p g^{\mu\nu} \, , \tag{1}$$

where $g^{\mu\nu}$ are the coefficients of the metric and are chosen to be those of a Schwarzschild spacetime in spherical coordinates (t, r, θ, ϕ). Here p, ρ, and h are the isotropic pressure, the rest-mass density, and the specific enthalpy, respectively. In the following the fluid will be modeled as ideal with a polytropic equation of state $p = \kappa \rho^\gamma$, where κ is the polytropic constant and γ the adiabatic index. The motion of the fluid is non-geodesic with four-velocity $u^\alpha = u^t(1, 0, 0, \Omega)$, where $\Omega = \Omega(r, \theta) \equiv u^\phi/u^t$ is the coordinate angular velocity as observed from infinity.

Under these assumptions, the equations of motion for the fluid can be generically written as $h^i{}_\nu \nabla_\mu T^{\mu\nu} = 0$ where $h_{\mu\nu} \equiv g_{\mu\nu} + u_\mu u_\nu$ is the projector tensor orthogonal to $\mathbf{u}$ and ∇ the covariant derivative in the Schwarzschild spacetime. Enforcing the conditions of hydrostatic equilibrium and of axisymmetry (i.e. $\partial_t = 0 = \partial_\phi$) simplifies the hydrodynamical equations considerably. Furthermore, if the contributions coming from the self-gravity of the torus can be neglected, the relativistic hydrodynamics equations reduce to Bernoulli-type equations

$$\frac{\nabla_i p}{e + p} = -\nabla_i W + \frac{\Omega \nabla_i \ell}{1 - \Omega \ell} \, , \tag{2}$$

where $i = r, \theta$ and $W = W(r, \theta) \equiv \ln(u_t)$. The local extrema of the potential $W = W(r, \theta) \equiv \ln(u_t)$ on the equatorial plane identify the positions of the two Keplerian points of the solution. At these locations an orbiting fluid element would not experience any acceleration coming from pressure gradients, the centrifugal force balancing the gravitational force exactly. These points correspond to the positions of the cusp, $r_{\rm cusp}$,
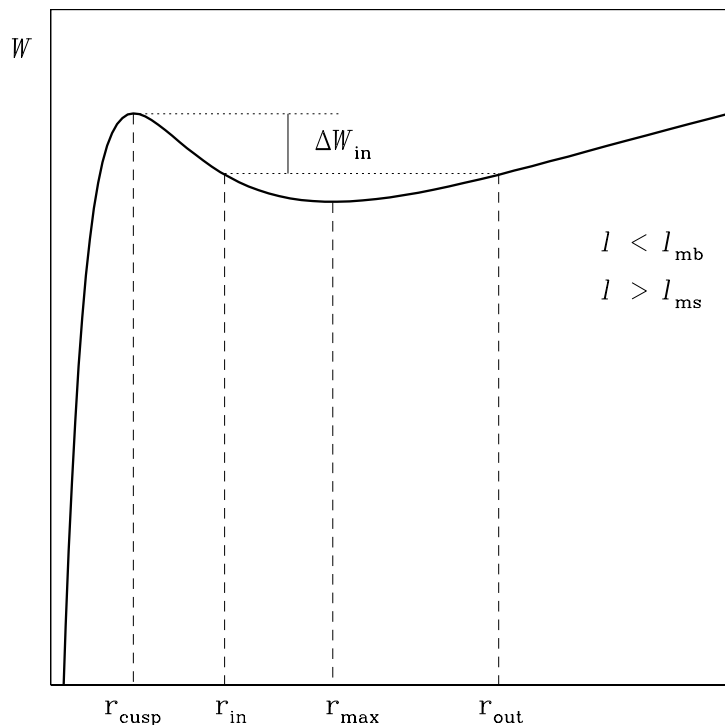

Figure 1. Potential $W = \ln(u_t)$ on the equatorial plane for a constant specific angular momentum distribution with $\ell_{\rm ms} < \ell < \ell_{\rm mb}$. The two extrema mark the position of the Keplerian points, namely the cusp, $r_{\rm cusp}$, and the maximum rest-mass density, $r_{\rm max}$, of the disc. The inner edge $r_{\rm in}$ can be chosen anywhere between $r_{\rm cusp}$ and $r_{\rm max}$. The energy gap $\Delta W_{\rm in} = W_{\rm in} - W_{\rm cusp}$ is used to fix $r_{\rm in}$.

and of the maximum rest-mass density (i.e. the "centre" of the torus) $r_{\rm max}$ (see Figure 1). While a detailed classification of the possible models can be found in the literature [1, 9], here I simply recall that different models for the tori will be determined after different

radial distributions for the specific angular momentum $\ell \equiv -u_\phi/u_t = \ell(r\sin\theta)$ (i.e. the angular momentum per unit energy) have been chosen.

An obvious and widely discussed choice for the specific angular momentum is the one in which the specific angular momentum is assumed to be constant inside the torus and in the range between the specific angular momentum at the marginally stable orbit $\ell_{\rm ms} = 3\sqrt{6}/3 \simeq 3.67$ and the one at the marginally bound orbit $\ell_{\rm mb} = 4$, to yield a disc of finite size. In this case then, the second term on the right-hand-side of equation (2) is zero and the Euler equations for a polytrope can be integrated analytically to yield the rest-mass density distribution inside the torus as

$$\rho(r,\theta) = \left(\frac{\gamma-1}{\kappa\gamma}\right)^{1/(\gamma-1)} [\exp(W_{\rm in} - W) - 1]^{1/(\gamma-1)} \ , \tag{3}$$

where $W_{\rm in} \equiv W(r_{\rm in}, \pi/2)$, $r_{\rm in}$ marking the inner edge of the torus. The models described so far represent the fiducial background fluid configurations.

3. Numerical setup

As shown by [10], the general relativistic Euler equations can be written as a hyperbolic system of conservation laws, which take the form [11]

$$\frac{\partial \mathbf{U}}{\partial t} + \frac{\partial [\alpha \mathbf{F}^r]}{\partial r} + \frac{\partial [\alpha \mathbf{F}^\theta]}{\partial \theta} = \mathbf{S} \ , \tag{4}$$

where $\alpha \equiv \sqrt{-g_{00}}$ is the lapse function of the Schwarzschild metric. Here, $\mathbf{U} = (D, S_r, S_\theta, S_\phi)$ is the state-vector of the "conserved" variables, namely the relativistic rest-mass density and the momenta in the coordinate directions, respectively. All of the quantities are as measured by an Eulerian observer in the Schwarzschild metric. The other vectors $\mathbf{F}^i$ and $\mathbf{S}$ appearing in (4) represent the fluxes and sources of the evolved quantities, respectively, with the latter being entirely due to the curvature of spacetime. Explicit expressions of all these terms can be found in [12].

The conservative nature of the system (4) is the key ingredient for the use of High-Resolution Shock-Capturing (HRSC) numerical methods which assure high-order accuracy, sharp resolution of discontinuities and absence of spurious oscillations everywhere in the solution, even at relativistic regimes. Such methods, which are also referred to as "Godunov-type" methods, have been employed in general relativistic calculations only rather recently but have shown their ability to yield results of unprecedented accuracy [13]. Within these methods, the time evolution of the discretized data from a timelevel n to the subsequent one $n + 1$ is made according to the following numerical scheme

$$\mathbf{U}_{i,j}^{n+1} = \mathbf{U}_{i,j}^n - \frac{\Delta t}{\Delta r}\left(\widehat{\mathbf{F}}_{i+1/2,j}^r - \widehat{\mathbf{F}}_{i-1/2,j}^r\right) - \frac{\Delta t}{\Delta\theta}\left(\widehat{\mathbf{F}}_{i,j+1/2}^\theta - \widehat{\mathbf{F}}_{i,j-1/2}^\theta\right) + \Delta t\, \mathbf{S}_{i,j} \ , \tag{5}$$

where the subscripts i, j refer to spatial (r, θ) gridpoints, so that $\mathbf{U}_{i,j}^n \equiv \mathbf{U}(r_i, \theta_j, t^n)$. The inter-cell numerical fluxes, $\widehat{\mathbf{F}}_{i\pm1/2,j}^r$ and $\widehat{\mathbf{F}}_{i,j\pm1/2}^\theta$, are computed using Marquina's approximate Riemann solver [14]. A piecewise-linear cell reconstruction procedure provides

second-order accuracy in space, while the same order in time is obtained with a two-step second-order Runge-Kutta scheme applied to evolution scheme in expression (5).

The computational grid, consisting typically of $N_r \times N_\theta = 250 \times 84$ zones in the radial and angular directions, respectively, covers a computational domain extending from $r_{\min} = 2.1$ to $r_{\max} = 30$ and from 0 to π. Moreover, in order to achieve the best resolution in the vicinity of the cusp, the radial grid is logarithmically spaced in terms of a tortoise coordinate $r_* = r + 2M \ln(r/2M - 1)$, with the maximum radial resolution at the innermost grid being $\Delta r = 6 \times 10^{-4}$.

4. Evolution of the spacetime

In order to assess the occurrence of the runaway instability, the changes in the spacetime must be taken into account. Ideally, this would require the solution of the Einstein equations as well as those of relativistic hydrodynamics. Besides the intrinsic difficulty of this problem and despite the fact that a number of numerical codes are being developed for this purpose, the need of high resolution is still the major obstacle to the goal.

Here, to avoid the solution of the full Einstein equations and yet simulate the evolution of the spacetime, a more pragmatic approach (already suggested by [9]) has been chosen. In practice, the metric terms are updated from a given timestep to the following one according to the amount of matter which has accreted into the hole, i.e.

$$g_{\mu\nu}(r, M^n) \longrightarrow \tilde{g}_{\mu\nu}(r, M^{n+1}) , \tag{6}$$

where $\tilde{g}_{\mu\nu}$ describes the spacetime at the timelevel $n+1$ and M^{n+1} is the "new" mass of the black hole as computed in terms of the accretion rate at the inner zone of the grid $\dot{m}^n(r_{\min})$

$$M^{n+1} = M^n + \Delta t \, \dot{m}^n(r_{\min}) , \tag{7}$$

where

$$\dot{m}(r_{\min}) \equiv -2\pi \int_0^\pi \sqrt{-g} D v^r d\theta \Big|_{r_{\min}} . \tag{8}$$

Simulations employing the time evolution of the metric (6) will be referred to as simulations with a *dynamical spacetime* to distinguish them from those simulations in which the black hole mass is not evolved, $M^{n+1} = M^n$, and that will be referred to as with a *fixed spacetime*.

Of course, the approach sketched in equation (6) is only an approximation which does not account for the transfer of angular momentum from the torus to the black hole and that prevents from the calculation of the response of the black hole to the accreted mass and the corresponding emission of gravitational radiation. Nevertheless, it can be considered a satisfactory one when the tori are not very massive and the rest-mass accretion rates are small.

5. Initial data

In previous simulations of an accreting torus over a fixed [15] or over an evolving [9] spacetime, a deviation from the stationary solution was obtained by artificially expanding

the torus by a small amount to overcome the potential barrier, thus setting the initial configuration out of equilibrium. The quantity controlling the deviation from equilibrium is the potential jump on the equatorial plane between the inner edge of the torus and the position of the cusp, and it is defined as $\Delta W_{\rm in} \equiv W_{\rm in} - W_{\rm cusp}$ (see Figure 1). Clearly, when $\Delta W_{\rm in} > 0$, the torus overflows its Roche lobe and accretion onto the black hole is not only possible, but rather unavoidable.

In calculations presented here, instead, all of the models have potential barriers $\Delta W_{\rm in} \leq 0$, and the departure from the equilibrium solution is obtained by introducing a perturbation in the radial velocity field, which is chosen as a homologous parametrization of the spherical accretion solution in a Schwarzschild spacetime, i.e. the Michel solution [16]. Using η to parametrize the strength of the perturbation, the initial radial (covariant) component of the three-velocity has been specified as

$$v_r = \eta (v_r)_{\rm Michel} \ , \tag{9}$$

where $(v_r)_{\rm Michel}$ is the radial component of the velocity in the Michel solution.

Doing so provides the possibility of testing how sensitive the runaway instability is on the specific initial conditions chosen and, in particular, on the assumption that the torus is already overflowing its Roche lobe. Furthermore, by having a nonzero initial radial velocity in addition to the orbital one, these initial conditions are more consistent with the results of a series of Newtonian simulations in which a torus is produced as a result of the dynamical merging of two neutron stars [17]. In these simulations, in fact, the torus is seen to maintain an averaged inflow velocity in the central region of the order of $\sim 3 \times 10^{-3}c$. The values of the parameter η have therefore been chosen such as to be compatible with the estimates provided by [17] and are in the range $[0.001, 0.06]$.

A small but representative sample of the equilibrium models considered in these simulations is reported in Table 1.

6. Numerical results

6.1. Runaway instability

Simulations performed in a dynamical spacetime (in the sense explained in Section 4) and using the initial conditions discussed in Section 5 have confirmed what found by [9], namely the occurrence of the runaway instability for constant angular momentum configurations. Moreover, the simulations have highlighted that Roche lobe overflowing is not a necessary condition for the development of the instability, which can therefore take place under a variety of different initial conditions as long as the distribution of specific angular momentum is maintained constant.

Figure 2 shows the evolution of the rest-mass accretion rate for model (a) in a dynamical spacetime (see Table 1) and for three different values of initial velocity perturbation, η. The time is expressed in terms of the orbital period $t_{\rm orb} \equiv 2\pi/\Omega_{\rm max}$ for a particle orbiting at the radial position of the maximum density in the torus, and which is $t_{\rm orb} = 1.87$ ms for all of the models in Table 1.

As it is apparent from the figure, the accretion rate grows exponentially after an amount of time which is shorter for larger values of the initial velocity perturbation. Furthermore, the secular growth in the rest-mass accretion rate is accompanied by regular,

Table 1. Main properties of the constant angular momentum relativistic tori used in the numerical calculations. From left to right the columns report: the name of the model, the torus-to-hole mass ratio M_t/M, the polytropic constant κ, the density at the "centre" of the torus and the average density of each model, respectively, both in cgs units. All of the models share the same mass for the black hole, $M = 2.5 M_\odot$, and the adiabatic index, $\gamma = 4/3$. The inner and outer radii, the radial position of the cusp and of the "centre" are also the same for these models, and are given by $r_{in} = 4.576$, $r_{out} = 15.89$, $r_{cusp} = 4.57$, $r_{max} = 8.35$, respectively, in units of $r_g \equiv GM/c^2$.

Model	M_t/M	κ (cgs)	ρ_{max} (cgs)	$\langle\rho\rangle$ (cgs)
(a)	1.00	4.46×10^{13}	1.14×10^{14}	4.72×10^{12}
(b)	0.50	5.62×10^{13}	5.72×10^{13}	2.36×10^{12}
(c)	0.10	0.96×10^{14}	1.14×10^{13}	4.73×10^{11}
(d)	0.05	1.21×10^{14}	5.73×10^{12}	2.36×10^{11}

periodic oscillations. As a consequence of the introduction of the initial perturbation, in fact, the torus experiences a series of compressions and expansions during which a considerable amount of matter falls towards the black hole. In the half-period of oscillation leading to the compression wave, in particular, the inner edge of the torus moves towards the black hole and a certain amount of matter can overcome the potential barrier, thus producing the local maxima in the accretion rate which are visible in Figure 2. Note also that the oscillations are not at constant amplitude, but have increasingly large amplitudes produced by the development of the instability. This superposition of the onset of the instability and of the response to the perturbation prevents a direct analysis of the periodic component; this difficulty, however, can be overcome simply as will be discussed in Section 6.2.

The calculations during the final stages of the instability become increasingly difficult because of the dramatical changes in the hydrodynamical quantities (note the exponential increases in Figure 2). In such conditions, Courant factors as small as 0.01 must be taken in order to avoid the crashing of the code. Soon after the accretion rate has reached its maximum, it drops rapidly to very small values as a consequence of the fact that 98% of the initial mass of the torus has accreted onto the hole by then.

When models with smaller mass ratios M_t/M are evolved [i.e. models (b), (c) and (d) in Table 1] the accretion rate is generally lower and the amount of matter accreted can be very small even over several tens of dynamical timescales. In these conditions the timescales for the onset and development of the instability are progressively larger, but all of the qualitative features discussed so far apply unmodified (see [8] for further details).
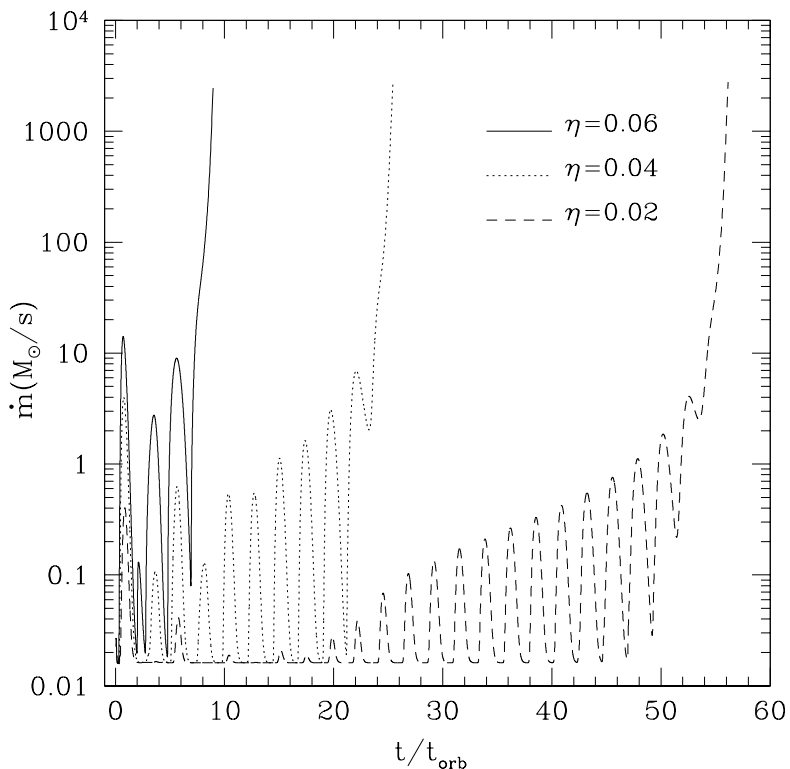
Figure 2. Evolution of the rest-mass accretion rate for model (a) and for different values of η when the spacetime is allowed to vary (i.e. a dynamical spacetime). The time is expressed in terms of the timescale for the "centre" of the toroidal neutron star to perform an orbit. Note that the onset and development of the instability is accompanied by periodic oscillations.

6.2. Quasi-Periodic Behaviour

When concentrating on the quasi-periodic response of the torus to perturbations, the occurrence of the runaway instability represents a complication to avoid. Since the occurrence of the instability itself is still under debate and could be suppressed when more generic initial conditions are considered (e.g. with a non-constant specific angular momentum distribution [18]), in the rest of the simulations presented here the spacetime has been maintained fixed, hence suppressing the onset of the runaway instability.

Figure 3 is the same as Figure 2, but shows the evolution of the accretion rate during the first 30 orbital periods for a simulation in which the spacetime is held fixed. As in the case of a dynamical spacetime, the amplitude of the rest-mass accretion rate shows a dependence on the strength of the initial perturbation, with $\dot{m}$ becoming progressively larger with increasing η. In these simulations, however, the accretion rate never diverges and the pulsating behaviour can therefore be studied more in detail. Each period of oscillation in Figure 3 is the result of several tens of thousands timesteps and the ability to preserve the periodic nature of the oscillations confirms the ability of HRSC methods in reproducing subtle hydrodynamical effects with very high precision. Note also that, as shown in the inset of Figure 3, the periodic behaviour is not altered even when observed over 100 orbital timescales, until the numerical simulation is stopped or the relativistic
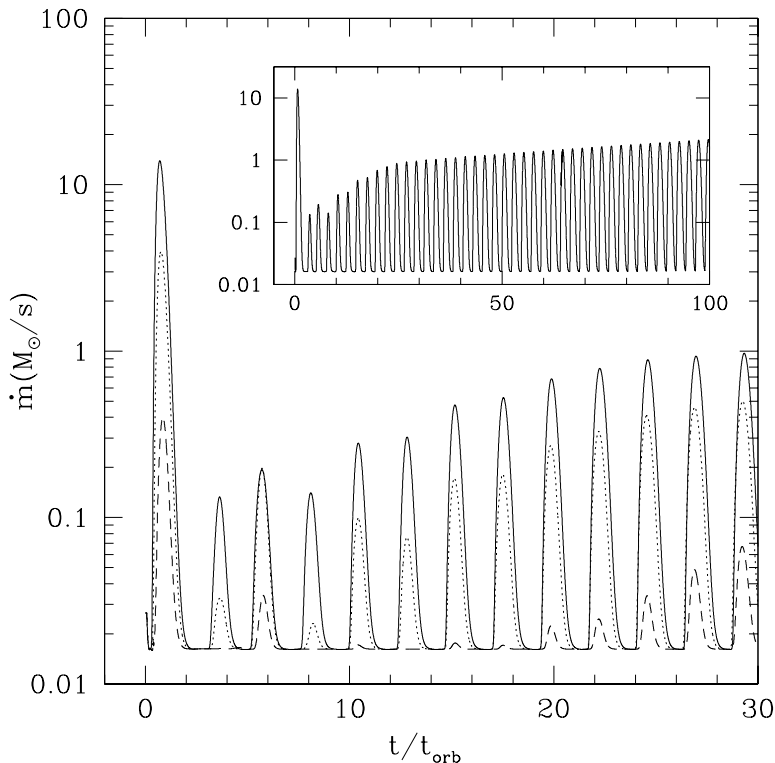
Figure 3. Rest-mass accretion rate in a fixed-spacetime evolution. The solid, dotted and dashed lines correspond to $\eta = 0.06, 0.04$, and 0.02, respectively. The inset shows the case $\eta = 0.06$ over a very long timescale (100 orbital periods).

torus has been entirely accreted by the black hole.

It is important to underline that the rest-mass accretion rate is not the only quantity showing a periodic behaviour and, indeed, all of the fluid variables can be shown to oscillate periodically. However, before presenting the physical interpretation of the oscillations detected, it is useful to quantify the quasi-periodicity observed in the simulations in terms of a Fourier analysis of some relevant hydrodynamical quantities. As a good representative case, Figure 4 shows the power spectrum of the L_2 norm of the rest-mass density (i.e. an integral quantity over the numerical grid) for models (a), (b) and (c) of Table 1. The Fourier transform has been calculated with data obtained with an $\eta = 0.06$ perturbation and computed over a time interval going up to $t/t_{\rm orb} \simeq 100$.

As it is evident from Figure 4, all of the three power spectra consist of a fundamental frequency f_0 (228 Hz for the models considered in Figure 4) and a series of overtones (at 340, 456 Hz, and so on) in a ratio which can be determined to be $2 : 3 : 4 : \ldots$, to an accuracy of a few percent. This clearly suggests that the quasi-periodic response observed is the consequence of fundamental modes of oscillation of the torus. While reminiscent of epicyclic oscillations, these modes cannot be interpreted in terms of radial perturbations of circular Keplerian orbits as the epicyclic frequency is zero for constant specific angular momentum distributions (This property holds in Newtonian gravity but has been shown to hold also in a relativistic regime [19].). These oscillations should indeed be interpreted in terms of *"p modes"* (or inertial-acoustic modes) of the torus.
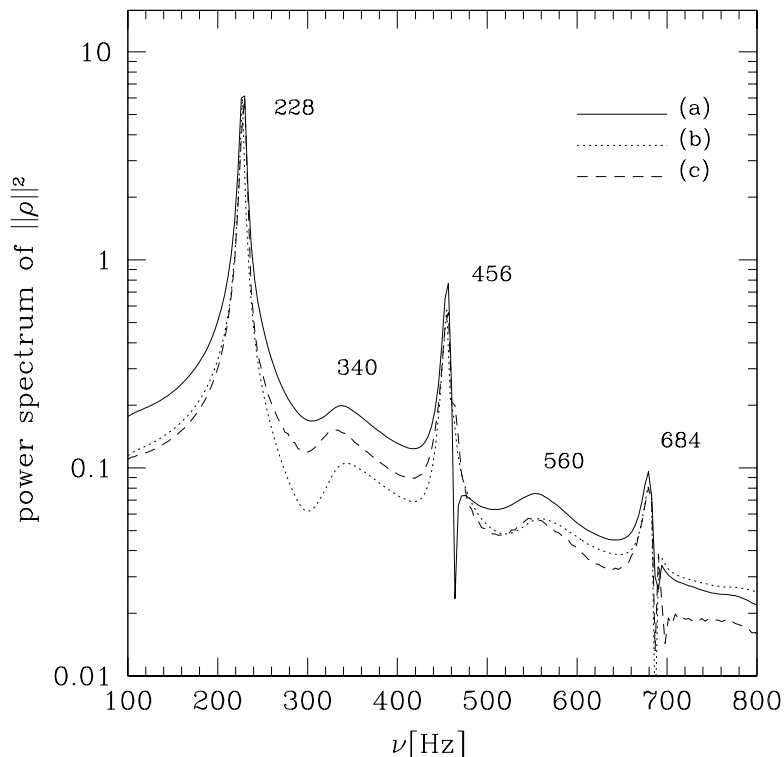
9

Figure 4. Power spectrum of the rest-mass accretion rate for models (a), (b), and (c) of Table 1. The values on the vertical axis have been suitably normalized to match the power in the fundamental mode and arbitrary units have been used.

To prove this, a detailed linear perturbative analysis has been performed [19], in which it has been shown that p modes in a general non-Keplerian disc represent the vibrational modes having pressure gradients as the restoring force, and appear with eigenfrequencies in the same sequence $2 : 3 : 4 : \ldots$ revealed here. A detailed discussion of the results of this perturbative analysis can be found in [19] and will not be further discussed here. However, a much simpler argument can be given to justify the interpretation of the oscillations detected as p modes. As a by-product of the assumption of constant specific angular momentum distributions, in fact, the sound speed is independent of the polytropic constant in these tori. Since the power spectra reported in Figure 4 refer to models having the same spatial extensions but differing in the values for the polytropic constant (and hence in the total rest-mass), they should all possess identical features if the oscillations are to reflect sound wave propagation in thick discs. Indeed, this is what shown in Figure 4, where all the frequencies differ for less than 0.1% despite the tori producing them have considerably different masses and hence different average densities.

The approach discussed here represents a first step towards a relativistic discoseismology analysis for massive and vertically extended tori in General Relativity. This is in close analogy to what has been extensively developed for geometrically thin discs [20, 21, 22, 23] and may serve as a guide to interpret astrophysical phenomena where thick discs play an important role.

6.3. Linear and Nonlinear Regimes

All of the quasi-periodic behaviour discussed so far is the consequence of the finite size perturbations that have been introduced in the initial configuration. Within this approach a *linear* regime is expected in which the response of the toroidal neutron star is linearly proportional to the perturbation introduced, and a *nonlinear* regime when this ceases to be true. The strength of the perturbation which marks the transition between the two regimes can be estimated from Figure 5, which shows the averaged maximum rest-mass density reached during the oscillations ρ_M, normalized to the value at the centre of the toroidal neutron star ρ_{max}.
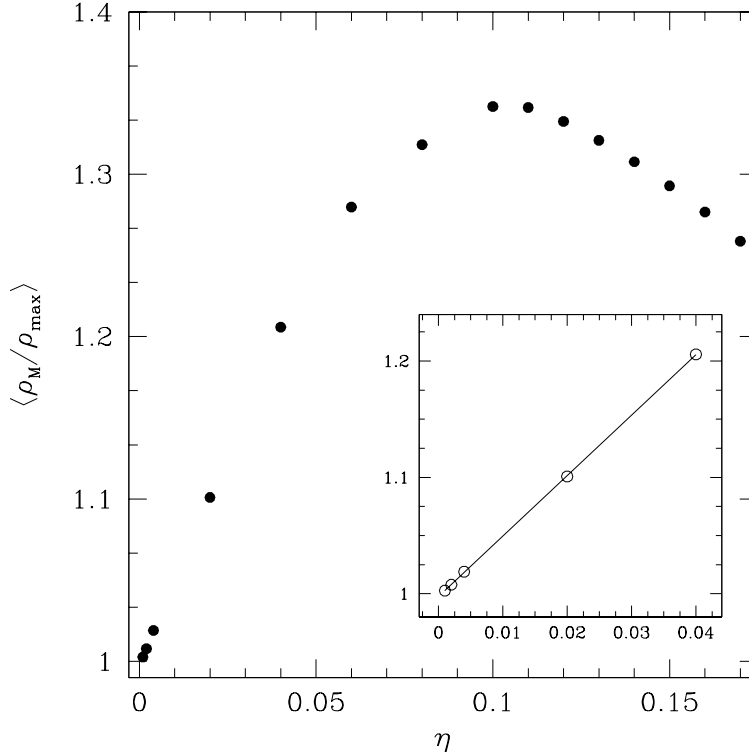

Figure 5. Averaged maximum rest-mass density normalized to the central one in the toroidal neutron star as a function of the perturbation strength. The small inset shows a magnification of the behaviour in the linear regime and the solid line shows the good linear fit to the data. The data refers to model (a) and has been averaged over 10 orbital timescales.

A rapid look at Figure 5 reveals the presence of both the linear and nonlinear regimes with the first one being shown magnified in the inset, and where the solid line shows the good linear fit to the data. The transition between the two regimes seems to occur for $\eta \simeq 0.05$, with the nonlinear regime producing maximum amplitudes that are $\sim 35\%$ larger than the initial one. A careful analysis of the behaviour of the fluid variables shows that for perturbations with strength $\eta \gtrsim 0.05$, some of the kinetic energy which is confined to the lower order modes in the linear regime, tends to be transferred also to higher order modes. The nonlinear coupling among different modes and the excitation of higher order overtones is often encountered in Nature where it serves to

redistribute the excess kinetic energy before the production of shocks. In practice, the nonlinear coupling deprives of energy the fundamental mode (which is the one basically represented in Figure 5) and is therefore responsible for the decay of $\langle \rho_{\mathrm{M}}/\rho_{\mathrm{max}} \rangle$ for $\eta \gtrsim 0.1$. Interestingly, when analysed in terms of the power spectra, this effect shows a very distinctive behaviour. As the nonlinear mode-mode coupling becomes effective, the amount of power in the fundamental mode becomes increasingly smaller as the strength of the perturbation is increased. At the same time, the conservation of energy transfers power to the overtones, with the first ones reaching amplitudes comparable to the fundamental one and with the high order ones becoming more and more distinct from the background.

Determining the transition to the nonlinear regime is important to set an approximate upper limit on the amplitude of the oscillations and is relevant when estimating the emission of gravitational waves. It should also be noted that in the parameter range for η in which the calculations have been performed (i.e. $\eta \in [0.001, 0.12]$), the peak frequencies in the power spectra have not shown to depend on the values used for η. This is of course consistent with them being fundamental frequencies (and overtones).

6.4. Gravitational Wave Emission

Although the present analysis is not able to calculate in a self-consistent manner the emission of gravitational waves produced by the linear and nonlinear dynamics of the torus, it is nevertheless interesting to attempt a first estimate of this. The rationale is that during the oscillations the tori undergo large and rapid variations of their mass quadrupole moments, which are intrinsically large for fluid configurations with high density and a toroidal topology. As a result, perturbed toroidal neutron stars undergoing periodic oscillations have the potential of being strong sources of gravitational waves.

In the Newtonian quadrupole approximation, the gravitational waveform $h^{TT}(t)$ observed at a distance R from the source can be calculated in terms of the quadrupole wave amplitude A_{20}^{E2} (see also [24])

$$h^{TT}(t) = F_+ \left(\frac{1}{8} \sqrt{\frac{15}{\pi}} \right) \frac{A_{20}^{\mathrm{E2}}(t-R)}{R} \, , \tag{10}$$

where $F_+ = F_+(R, \theta, \phi)$, the detector's beam pattern function, is assumed to be optimal, i.e. $F_+ = 1$. The wave amplitude A_{20}^{E2} in Eq. (10) is the second time derivative of the mass quadrupole moment $A_{20}^{\mathrm{E2}} = d^2I/dt^2$, where I is defined as

$$I \equiv \int \rho \left(\frac{3}{2}z^2 - \frac{1}{2} \right) r^4 dr dz \, , \tag{11}$$

with $z \equiv \cos\theta$.

Within this Newtonian framework and using the results of the numerical calculations to estimate the gravitational wave amplitude, it is then possible to derive a phenomenological expression for the gravitational waveform that could be expected as a result of the oscillations induced in the torus. In particular, a source with mass M_{t} and located somewhere in the Galaxy (i.e. at a distance $R = 10$ Kpc), would produce a transverse traceless gravitational wave amplitude given by

$$h^{TT} \simeq 2.2 \times 10^{-21} \left(\frac{\eta}{0.04} \right) \left(\frac{M_{\mathrm{t}}}{0.1 \, M_{2.5}} \right) \left(\frac{10 \, \mathrm{Kpc}}{R} \right) \, , \tag{12}$$
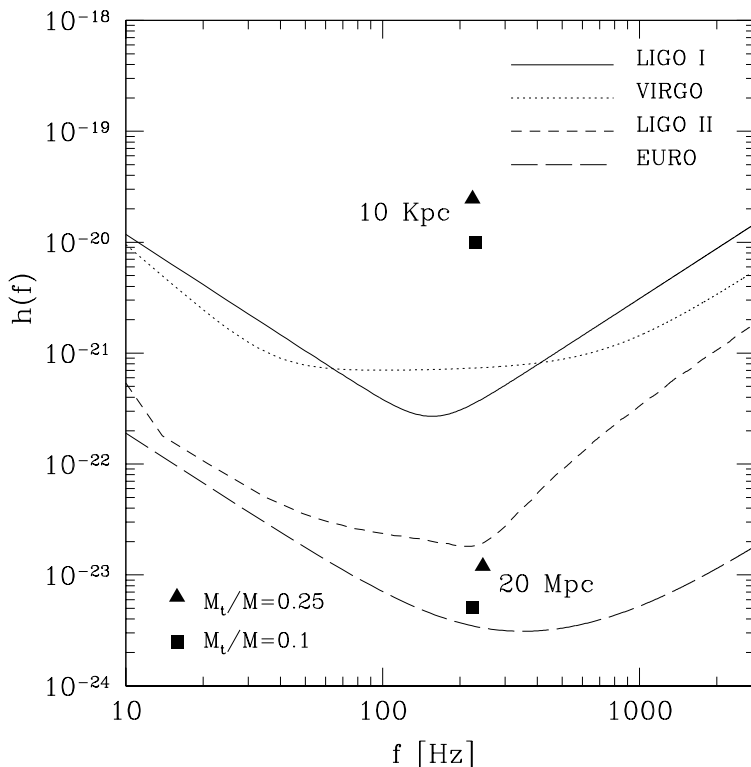
Figure 6. Characteristic wave amplitudes for a perturbed toroidal neutron star with $\eta = 0.04$. These amplitudes have been computed using the strain noise estimated for LIGO I for a source located at a distance of 10 Kpc and for LIGO II for a source at a distance of 20 Mpc. The numbers can also be compared with the sensitivity curves of VIRGO and EURO that are similar in this frequency range. Different points refer to different mass ratios, with triangles indicating $M_t/M = 0.25$ and squares $M_t/M = 0.1$.

where $M_{2.5} \equiv M/(2.5\ M_\odot)$. Expression (12) shows that, already in the linear regime, a non-negligible gravitational wave amplitude can be produced by an oscillating toroidal neutron star orbiting around a black hole. This amplitude is comparable with the average gravitational wave amplitude computed in the case of core collapse in a supernova explosion [24, 25] and can become stronger for larger perturbations or masses in the torus.

In order to quantify the detectability of relativistic tori by present and planned the interferometric detectors, it is necessary to compute the *characteristic* gravitational wave frequency and amplitude, as well as the corresponding signal-to-noise ratio for these detectors. More specifically, these quantities have been evaluated following the procedure discussed in [8] and use, for a "realistic" toroidal neutron star model with mass $M_t/M = 0.1$ and $\eta = 0.04$, a representative timescale $\tau_{\rm life} = 0.18$ s. Longer (shorter) timescales are instead assumed for models with smaller (larger) initial perturbations (cf. Table 2).

Figure 6 and Table 2 show a small but significant fraction of the parameter space investigated by the numerical simulations. Figure 6, in particular, shows the characteristic wave amplitude for sources located at a distance of $R = 10$ Kpc and $R = 20$

13

Table 2. Characteristic properties for the detection of the gravitational wave signal emitted by a toroidal neutron star. The first two columns show the mass of the toroidal neutron star normalized to the black hole one, as well as the strength of the initial perturbation η. The following three columns report the signal-to-noise ratio computed for LIGO I, LIGO II and EURO, assuming a galactic distance (third column) or an extragalactic one (fourth and fifth columns) . The last column reports the characteristic lifetime for the existence of relativistic tori that are unstable to the runaway instability. Of course, a toroidal neutron star may survive longer than this timescale should the runaway instability not occur.

M_{t}/M	η	S/N LIGO I (10 Kpc)	S/N LIGO II (20 Mpc)	S/N EURO (20 Mpc)	τ_{life} (s)
0.10	0.06	23.2	0.1	1.8	0.14
0.10	0.04	19.9	0.1	1.5	0.18
0.10	0.02	11.9	< 0.1	0.9	0.20

Mpc, as computed for two different values of the torus-to-hole mass ratio. These amplitudes have been computed for the expected strain noise of LIGO I and LIGO II, but the strain curves of VIRGO (that is similar in this frequency range, [26]) and of EURO [27] have also been reported for comparison. Interestingly, with small initial perturbations ($\eta = 0.04$) and mass ratios ($M_{\mathrm{t}}/M = 0.1$), the computed characteristic amplitudes can be above the sensitivity curves of LIGO I for sources within 10 Kpc and above the sensitivity curve of EURO for sources within 20 Mpc. Both results suggest that a relativistic torus oscillating in the Virgo cluster could be detectable by the present and planned interferometric detectors.

Table 2 provides a more quantitative measure of the likelihood of the detection of toroidal neutron stars as sources of gravitational waves by reporting the signal-to-noise ratios as computed for LIGO I, LIGO II and EURO, as well as the timescale over which the signal has been computed. All of these quantities refer to models with different initial perturbations and located at either 10 Kpc (for LIGO I) or 20 Mpc (for LIGO II and EURO). As it is apparent from the table, even an extragalactic source with a small amount of perturbations could emit a gravitational wave signal strong enough to be detected by the planned detector EURO.

7. Conclusions

I have presented general relativistic hydrodynamics simulations of relativistic axisymmetric tori orbiting around a Schwarzschild black hole with a constant specific angular momentum. The simulations make use of HRSC methods and are able to reproduce faithfully both the linear and the nonlinear response of the relativistic tori. There are three main aspects of this research that are worth to be highlighted.

The first one concerns the issue of the runaway instability, a dynamical instability which is expected to take place when a geometrically thick disc accretes matter onto

a black hole through the cusp of its outermost equipotential surface. The calculations reported here for a variety of different models show that, at least for constant specific angular momentum tori whose self-gravity is neglected, the runaway instability represents a robust, unavoidable feature of their dynamics. Furthermore, these simulations clarify that an initial Roche lobe overflow is not a necessary condition for the development of the instability.

The second aspect concerns the dynamical response of these relativistic tori to the perturbations that will be present when these objects form. Upon the introduction of suitably parametrized perturbations, the tori have shown a regular oscillatory behaviour resulting both in a quasi-periodic variation of the rest-mass accretion rate as well as of the rest-mass distribution. This response is to be interpreted in terms of the excitation of p modes having pressure gradients as restoring forces and appearing with eigenfrequencies in the sequence $2 : 3 : 4 : \ldots$.

Finally, as a consequence of the excitation of oscillations, the mass quadrupoles are induced to change rapidly and intense gravitational radiation is thus produced. Estimates made within the Newtonian quadrupole approximation have shown that strong gravitational waves can be produced during the short lifetime of these tori. In particular, the gravitational radiation emitted by these sources is comparable or larger than the one that is expected during the gravitational collapse of a stellar iron core, with a rate of detectable events which could also be larger given the variety of physical scenarios leading to the formation of a massive torus orbiting a black hole.

Acknowledgments

References

[1] Abramowicz M. A. Jaroszyński M. & Sikora M., 1978, A&A, 63, 221.

[2] Kozlowski M., Jaroszynski M., Abramowicz M. A., 1978, A&A, 63, 209

[3] Abramowicz M. A., Calvani M., Nobili L., 1983, Nature, 302, 597

[4] Daigne F., Mochkovitch R., 1997, MNRAS, 285, L15

[5] Meszaros P., 2002, ARA&A, 40, 137

[6] van der Klis M., 2000, ARA&A, 38, 71

[7] Van Putten M. H., 2001, Phys. Rep. 345, 1

[8] Zanotti O., Rezzolla L., Font A. J., 2003, MNRAS, *in press*

[9] Font J. A., Daigne F., 2002a, MNRAS, 334, 383

[10] Martí, J.M., Ibañez, J. M., Miralles, J. A. 1991, Phys. Rev. D 43, 3794

[11] Banyuls F., Font J. A., Ibáñez J. M., Martí J. M., Miralles J. A., 1997, ApJ, 476, 221

[12] Font J. A., Ibáñez J. M., 1998a, ApJ, 494, 297

[13] Font J. A., Goodale T., Iyer S., Miller M., Rezzolla L., Seidel E., Stergioulas N., Suen W., Tobias M., 2002, Phys. Rev. D 65, 084024

[14] Donat R., Marquina A., 1996, J. Comp. Phys., 125, 42

[15] Igumenshchev I. V., Beloborodov A. M., 1997, MNRAS, 284, 767

[16] Michel F., 1972, Astrophys. Spa. Sci., 15, 153

[17] Ruffert M., Janka H.-T., 1999, A&A, 344, 573

[18] Font J. A., Daigne F., 2002b, ApJ, 581, L23

[19] Rezzolla L., Yoshida S'i., Zanotti O., 2003, MNRAS *submitted*

[20] Kato S., 2001, PASJ, 53, 1

[21] Perez C. A., Silbergleit A. S., Wagoner R. V., Lehr D. E., 1997, ApJ, 476, 589

[22] Silbergleit A. S., Wagoner R. V., Rodriguez M. O., 2001, ApJ, 548, 335

[23] Rodriguez M. O., Silbergleit A. S., Wagoner R. V., 2002, ApJ, 567, 1043

[24] Zwerger T., Müller E., 1997, A&A, 320, 209

[25] Dimmelmeier H., Font J. A., Müller E., 2002, A&A, 393, 523

[26] Damour T., Iyer B. R., Sathyaprakash B. S. 2001, Phys. Rev. D, 63, 044023

[27] Winkler W., for "The VIRGO/GEO Collaboration", Vision document www.astro.cf.ac.uk/geo/euro/